Original Article

ROS-Responsive siFGF19 Delivery Reprograms Pancreatic Stellate Cells and Remodels the Desmoplastic Microenvironment in Pancreatic Cancer

Zhaohong Wang[1,2,†], Shengzhang Lin[3,4,†], Suhua Zheng[1,5], Zhengrong Tian[1,6], Xihao Zhong[1], Xinchang Zhang[1], Shaodong Lin[1], Beier Wang[1], Yilun Xie[1], Hongfei Tong[1,7], Qiyu Zhang[1,2,*] and Zhonglin Ni[1,*]

[1]Department of Hepatobiliary and Pancreatic Surgery, The Second Affiliated Hospital of Wenzhou Medical University, 325000 Wenzhou, Zhejiang, China
[2]Department of Hepatobiliary and Pancreatic Surgery, The First Affiliated Hospital of Wenzhou Medical University, 325035 Wenzhou, Zhejiang, China
[3]Department of Hepatobiliary and Pancreatic Surgery, Shulan (Boao) Hospital, 571434 Qionghai, Hainan, China
[4]Department of Clinical Medicine, School of Medicine, Hangzhou City University, 310015 Hangzhou, Zhejiang, China
[5]Department of General Surgery, The People's Hospital of Pingyang, 325400 Wenzhou, Zhejiang, China
[6]Department of General Surgery, The Second Affiliated Hospital of Shaanxi University of Chinese Medicine, 712000 Xianyang, Shaanxi, China
[7]Department of Hepatobiliary and Pancreatic Surgery, Yongkang First People's Hospital of Wenzhou Medical University, 321300 Yongkang, Zhejiang, China
[†]These authors contributed equally.

Abstract

Background: Pancreatic ductal adenocarcinoma (PDAC) is characterized by extensive stromal fibrosis that limits drug delivery and promotes therapeutic resistance. Pancreatic stellate cells (PSCs), key mediators of desmoplasia, represent a promising yet underexploited therapeutic target. This study aimed to suppress PSC activation and remodel tumor stroma by silencing fibroblast growth factor 19 (FGF19) using a reactive oxygen species (ROS)-responsive small interfering RNA (siRNA) delivery system. **Methods**: A ROS-sensitive gold nanoparticle-based nanoplatform was constructed and characterized by transmission electron microscopy and dynamic light scattering. Cellular uptake, gene silencing, and functional effects were evaluated in human PSCs (hPSCs). Fibrosis-related markers were analyzed by Western blot and quantitative polymerase chain reaction. *In vivo* biodistribution, safety, and antitumor efficacy were assessed in a PANC-1 xenograft model. **Results**: The nanoplatform exhibited efficient siRNA loading, stability, and ROS-triggered release. Compared with free siRNA, it significantly enhanced intracellular delivery and FGF19 silencing in hPSCs. This resulted in reduced PSC activation, proliferation, migration, and invasion, along with increased apoptosis under oxidative stress. Expression of profibrotic markers, including α-smooth muscle actin, collagen I, and fibronectin, was markedly downregulated. *In vivo*, the nanoplatform preferentially accumulated in tumors, showed favorable biosafety, and significantly inhibited tumor growth. **Conclusions**: ROS-responsive siFGF19 nanotherapy effectively reprograms PSC activation and remodels the fibrotic tumor microenvironment in PDAC. This strategy provides a promising approach for overcoming stromal barriers and improving therapeutic outcomes in pancreatic cancer.

Keywords: Pancreatic cancer, nanoparticle, pancreatic fibrosis, ROS-responsive.

***Address for correspondence**: Zhonglin Ni, Department of Hepatobiliary and Pancreatic Surgery, The Second Affiliated Hospital of Wenzhou Medical University, 325000 Wenzhou, Zhejiang, China. E-mail: nzl@wzhealth.com; Qiyu Zhang, Department of Hepatobiliary and Pancreatic Surgery, The Second Affiliated Hospital of Wenzhou Medical University, 325000 Wenzhou, Zhejiang, China; Department of Hepatobiliary and Pancreatic Surgery, The First Affiliated Hospital of Wenzhou Medical University, 325035 Wenzhou, Zhejiang, China. E-mail: qiyuz@126.com.

Introduction

Pancreatic ductal adenocarcinoma (PDAC) is the most common exocrine tumor and the most prevalent form of pancreatic cancer, accounting for over 90% of cases [1,2]. PDAC is a poorly vascularized malignant tumor characterized by a pronounced fibrotic stroma reaction, which is a hallmark of its microenvironment. This extensive fibrotic stroma comprises extracellular matrix proteins, small blood vessels lined with endothelial cells, and a variety of non-tumor cells (such as stellate cells and tumor-associated macrophages) along with the numerous cytokines they secrete, constituting approximately 90% of the total tumor volume [3–5]. Studies have shown that activated pancreatic stellate cells (PSCs) are the key effector cells mediating the fibrotic stroma response, playing a crucial role in maintaining pancreatic cancer fibrosis. Activated PSCs produce large amounts of extracellular matrix components such as collagen and fibronectin (FN), leading to significant pancreatic fibrosis [4]. They also release various growth factors and cytokines, which, through paracrine and autocrine mechanisms, further promote the proliferation and survival of tumor cells [6–8]. Therefore, reprogramming PSC activation rather than simply targeting tumor cells has emerged as a promising therapeutic paradigm for PDAC.

Fibroblast growth factor 19 (FGF19) is a crucial hormone-like fibroblast growth factor that regulates various cellular physiological functions and metabolism [9]. Studies have reported that FGF19 promotes cellular proliferation, with its murine homolog, Fgf15, inducing hepatocellular carcinoma and fibrosis in mice [10]. FGF19 activates signaling pathways that drive the rapid growth and invasion of tumor cells into surrounding tissues while collaborating with HMGA1 to form a dense, fibrous, scar-like stromal barrier encasing the tumor cells [11]. This stroma is thought to form a barrier that hinders therapeutic agents from reaching the tumor cells. Disruption of FGF19 signaling in pancreatic cancer mouse models has been shown to significantly reduce tumor cell growth and stroma formation. However, the potential of targeting FGF19 within PSCs to disrupt the fibrotic tumor microenvironment remains largely unexplored.

RNA interference (RNAi)-based therapeutics, particularly small interfering RNA (siRNA), offer a highly specific strategy for silencing disease-driving genes such as FGF19 [12,13]. Despite their therapeutic promise, clinical translation of siRNA is significantly hindered by poor stability, rapid degradation, and limited intracellular delivery [14]. Nanocarrier-based delivery systems have been developed to overcome these challenges, among which gold nanoparticles (Au NPs) have attracted considerable attention due to their tunable physicochemical properties, biocompatibility, and capacity for efficient nucleic acid loading [15–18]. Moreover, the tumor microenvironment is enriched with making reactive oxygen species (ROS), ROS-responsive carriers exhibit good tumor targeting ability. ROS-responsive linkers, such as thioketal (TK) bonds, can undergo cleavage in oxidative environments, enabling site-specific drug release [19–23]. Leveraging this feature, ROS-responsive nanocarriers have emerged as a promising strategy to achieve controlled and targeted delivery of therapeutic agents within the tumor microenvironment.

Based on these considerations, we hypothesized that a ROS-responsive siRNA nanodelivery system targeting FGF19 could selectively release therapeutic payloads within the tumor microenvironment, thereby reprogramming PSC activation and alleviating stromal fibrosis in PDAC. In this study, we developed a ROS-responsive gold nanoparticle-based nanoplatform for efficient delivery of siFGF19. We systematically evaluated its physicochemical properties, ROS-responsiveness, and gene silencing efficiency, as well as its ability to modulate PSC activation, remodel the fibrotic microenvironment, and inhibit tumor growth both *in vitro* and *in vivo*. Our findings provide a novel strategy for targeting stromal components in PDAC and highlight the therapeutic potential of microenvironment-responsive RNAi nanomedicine.

Materials and Methods

Materials

$HAuCl_4 \cdot 3H_2O$ (G141105), poly(ethyleneimine) solution (P434395), ascorbic acid (A656912), HEPES buffer solution (H433402), NaCl (S433747), N-hydroxy succinimide (NHS, H109330), N-(3-Dimethylaminopropyl)-N′-ethylcarbodiimide hydrochloride (EDC·HCl, E106172), and Cyanine 5 (Cy5) fluorescent dye (C196716) were all purchased from Aladdin (Shanghai, China). The ROS-responsive nanodrug carrier, methoxy polyethylene glycol (mPEG)-TK (R-00mTK-2k), was obtained from Xi'an Ruixi Biological Technology (China). siFGF19 was synthesized by RiboBio (Guangzhou, Guangdong, China).

Preparation of mPEG-TK-Au@siFGF19 (mPTAs)

Three candidate siRNAs targeting different coding regions of FGF19 were evaluated for gene-silencing efficiency. The detailed siRNA sequences and target regions are provided in **Supplementary Table 1**. Knockdown efficiency was initially assessed by reverse transcription quantitative polymerase chain reaction (RT-qPCR) and further confirmed by Western blotting. Cell viability was evaluated using the Cell Counting Kit-8 (CCK-8) assay to exclude nonspecific cytotoxicity. Among the three candidate siRNAs, siFGF19#3 exhibited the highest knockdown efficiency without affecting cell viability and was therefore selected for nanoparticle loading and all subsequent experiments.

The synthesis flask was added with 25 μL of 1% $HAuCl_4 \cdot 3H_2O$ solution and 2.5 mL of H_2O and stirred for 2 minutes. After thorough mixing, 1.5 mL of poly(ethyleneimine) solution (2.5 mg/mL) was added, and stirring continued for 5 minutes until the solution turned

pale yellow. Then, 80 μL of 0.1 mol/L ascorbic acid was added, and stirring was continued. After 5 minutes, the solution became transparent and colorless, followed by turning purple-red within 1 hour. The reaction was allowed to proceed for 24 hours to obtain Au NPs. The Au NPs solution was concentrated to 60 nM by centrifugation (14,000 rpm, 10 min).

siFGF19 was dissolved in 10 mM HEPES buffer solution (pH 7.2) to achieve a molar ratio of [siFGF19]/[Au NPs] = 360 and maintained at pH 7.2, with incubation at 4 °C for 8 hours. Then, 2 M NaCl was added to the solution (final NaCl concentration of 150 mM), and the solution was further incubated for 8 hours. Unbound siFGF19 was removed by repeated centrifugation (14,000 rpm, 10 min) in 10 mM HEPES buffer solution (pH 7.2) containing 150 mM NaCl, resulting in Au@siFGF19. mPEG-TK (700 mg), NHS (30 mg), EDC·HCl (45 mg), and Au@siFGF19 were dissolved separately in 10 mM HEPES buffer solution (pH 7.2) and mixed. The mixture was then incubated at 4 °C for 24 hours. Finally, mPTAs was dispersed in 10 mM HEPES buffer solution (pH 7.2) containing 150 mM NaCl, with the concentration of Au NPs being 11 nM.

Characterization

The structure and morphology of the samples were characterized using transmission electron microscopy (TEM, Talos F200X, FEI, Hillsboro, Oregon, USA). The mPEG-TK conjugate was characterized by ^{1}H NMR spectroscopy in $CDCl_3$. The particle size and zeta potential of the samples were measured using a nanoparticle sizer (Zetasizer Nano ZS, Malvern, Worcestershire, UK), and the effect of treatment with 0, 0.1, 0.5, 1, 5, and 10 mM H_2O_2 for 4 h on the particle size of the material was assessed. The ability of mPTAs to encapsulate siFGF19 was evaluated using gel electrophoresis with different weight ratios [mPEG-TK-Au (mPTA)]: siFGF19 = 0:1, 0.5:1, 1:1, 2:1, 5:1, 10:1, as well as under RNase and H_2O_2 stimulation. Gel electrophoresis analysis was performed by taking the mPTAs solution (1% agarose gel, 1 TBE buffer, 100 V, 15 minutes). After staining with SYBR Green II (K1070, APExBIO, Houston, Texas, USA), molecular imaging was conducted using an Molecular Imager (FX, BIO-RAD, USA; Ex/Em: 488/530) equipped with Quantity One software (version 4.6.2, Bio-Rad, Hercules, California, USA). mPTAs NPs were prepared according to the original method, except that siFGF19 was replaced with FAM-siFGF19. The resulting NPs were mixed with H_2O_2 at different concentrations (0, 0.1, or 1.0 mM) and incubated under stirring at 37 °C. At predetermined time points (0, 2, 6, 12, and 24 h), 100 μL aliquots were withdrawn and centrifuged at 14,000 rpm for 10 min. The supernatant was carefully collected, and its fluorescence intensity was measured using a fluorescence microplate reader (Synergy Neo2, BioTek, Winooski, Vermont, USA). The cumulative release percentage was calculated as follows: Release rate (%) = (fluorescence intensity of supernatant/total fluorescence intensity) × 100. The morphology of mPTAs after incubation with 0.1 mM H_2O_2 for 24 h was further examined by TEM.

Cell Culture

Human pancreatic stellate cells (hPSCs, HUM-iCell-g003), human umbilical vein endothelial cells (HUVECs, iCell-h110), and human pancreatic cancer cells PANC-1 (iCell-h172) were purchased from iCell Bioscience Inc. (Shanghai, China). hPSCs were cultured in DMEM (high glucose, PM150210, Procell, Wuhan, Hubei, China) supplemented with 10% fetal bovine serum (FBS). PANC-1 cells were cultured in DMEM basal medium containing 15% premium fetal bovine serum, 1% GlutaMAX-1, and 1% penicillin-streptomycin. Cells were maintained in a humidified atmosphere at 37 °C with 5% CO_2.

H_2O_2 Intervention and Administration Treatment

hPSCs were seeded into a 96-well plate at a density of 2×10^5 cells per well and cultured for 48 hours. Subsequently, the cells were treated with varying concentrations of mPTA NPs at 0, 10, 20, 50, 75, 100, and 150 μg/mL for 24 hours. Cell viability was assessed using the CCK-8 assay to confirm the cytotoxicity of the mPTA material itself. For further screening experiments, different concentrations of H_2O_2 (0, 25, 50, 100, 200, and 400 μM) and mPTAs (0, 10, 20, 50, 75, 100, and 150 μg/mL) were tested for cell viability, which was also analyzed using the CCK-8 assay.

hPSCs were divided into five groups: Control group: cells were untreated; Model group: cells were treated with 100 μM H_2O_2 for 24 hours; siFGF19 group, mPTA group, and mPTAs group: cells were treated as in the model group and then replaced with the corresponding drug (50 μg/mL) and continued to incubate for 24 hours.

CCK-8

Cell viability was assessed using the CCK-8 (E606335, Sangon Biotech, Shanghai, China). hPSCs were seeded into 96-well plates at a density of 1×10^4 cells per well in 100 μL of culture medium and incubated for 24 hours. Following incubation, various test agents were added for treatment, with three replicate wells for each group. After an additional 24 hours of incubation, 10 μL of CCK-8 reagent was added to each well, and the plates were incubated in the dark for another 2 hours. The absorbance at 450 nm was measured using a microplate reader to calculate cell viability. The CCK-8 assay was also used to evaluate the proliferation capacity of the cells in the aforementioned groups. Each experiment was repeated three times, and the mean values were recorded.

Cellular Uptake

To improve visualization, siFGF19 was labeled with the far-red fluorescent dye Cy5 (649/670 nm excitation/emission) at the 5' end of the sense strand to obtain

Cy5-siFGF19. For cellular uptake studies, hPSCs were seeded at a density of 10^5 cells per well in 20 mm confocal dishes and cultured for 24 hours. The cells were then incubated with either free Cy5-siFGF19 or mPTA@Cy5-siFGF19 (equivalent to 100 nM Cy5-siFGF19) in culture medium at 37 °C for 4 hours. After incubation, the cells were washed with PBS (BL302A, Biosharp, Hefei, Anhui, China) and fixed in 4% paraformaldehyde (PFA, P1110, Solarbio, Beijing, China) solution for 15 minutes. The cells were counterstained with DAPI and imaged using a confocal microscope (LSM710, Carl Zeiss, Oberkochen, Baden-Württemberg, Germany) with a 633 nm laser excitation.

Lysosomal Colocalization Assay

To evaluate intracellular trafficking and lysosomal escape of siRNA, lysosomal colocalization experiments were performed. hPSCs were seeded in confocal dishes and incubated with Cy5-labeled siFGF19-loaded nanoparticles for 4 h or 8 h. At each time point, the culture medium was removed, and cells were washed with PBS, followed by incubation with LysoTracker Green at 37 °C for 30 min. After washing with PBS, nuclei were stained with DAPI. Cells were immediately imaged using confocal laser scanning microscopy.

Western Blot

After 36 hours of intervention culture, cells were collected by centrifugation and lysed with an appropriate amount of radioimmunoprecipitation assay (RIPA) lysis buffer (P0013B, Beyotime, Shanghai, China). The cells were oscillated 3–4 times within 20 minutes at low temperature to ensure thorough lysis, followed by centrifugation at 13,000 rpm for 15 minutes to collect the supernatant. Total protein concentration was measured using a BCA Protein Assay Kit (P0012, Beyotime, Shanghai, China). Fibrosis marker proteins FN, collagen type I alpha 1 (Col-1α1), and α-smooth muscle actin (α-SMA) were detected using conventional Western blotting, with β-actin serving as the internal control. Anti-FN antibody (ab2413) was purchased from Abcam (Cambridge, UK), while anti-Col-1α1 (PB0981), α-SMA (BM3902), and β-actin (M01263-6) antibodies were obtained from Boster (Wuhan, Hubei, China). Enhanced chemiluminescence (ECL, K1129, APExBIO, Houston, Texas, USA) was used for detection, followed by exposure and development. Each experiment was repeated three times. Scanning images were analyzed using ImageJ software (1.50i, NIH, Bethesda, Maryland, USA), with the relative protein expression levels determined by the ratio of the grayscale value of the target band to that of the internal control band.

Immunofluorescence Staining of α-SMA

To verify α-SMA expression at the cellular level, immunofluorescence staining was performed. hPSCs were seeded in confocal dishes and subjected to the indicated treatments. After fixation with 4% PFA, cells were permeabilized with 0.1% Triton X-100 and blocked with 5% BSA for 30 min. Cells were then incubated overnight at 4 °C with anti-α-SMA primary antibody (14395-1-AP, Proteintech, Wuhan, Hubei, China). After washing with PBS, samples were incubated with fluorescent secondary antibody for 1 h at room temperature in the dark. Nuclei were counterstained with DAPI, and images were acquired using a confocal laser scanning microscope.

RT-PCR

Total RNA from hPSCs was extracted using Trizol reagent (15596026, Invitrogen, Carlsbad, California, USA). The extracted RNA was reverse-transcribed into cDNA using the TransScript All-in-One First-Strand cDNA Synthesis SuperMix for qPCR kit (AT321-01, Transgen, Beijing, China). The cDNA was then used as a template for RT-qPCR to detect mRNA expression levels. The primer sequences were as follows: FGF19: 5′-CAGAGCGCGCACAGTTTG-3′R, Reverse 5′-GCGGATCTCCTCCTCGAAAG-3′; FN: Forward 5′-AGGAAGCCGAGGTTTTAACTG-3′, Reverse 5′-AGGACGCTCATAAGTGTCACC-3′; Col-1α1: Forward 5′-CCGAGGCTCTGAAGGTCCC-3′, Reverse 5′-AGCAATACCAGGAGCACCATTG-3′; α-SMA: Forward 5′-GCTACCCGCCCAGAAACTAGA-3′, Reverse 5′-ACCCATACCGACCATGACG-3′. GAPDH was used as an internal reference, and the primer sequences were: Forward 5′-GGTCGGAGTCAACGGATTTG-3′, Reverse 5′-ACAAGCTTCCCGTTCTCAGC-3′. PCR reaction conditions: 95 °C for 3 min, 95 °C for 7 s, 57 °C for 10 s, and 72 °C for 15 s, 45 cycles. Ct values were obtained using the software provided by the PCR machine. The relative mRNA expression levels were calculated using the $2^{-\Delta\Delta CT}$ method.

Assessment of Migration and Invasive Capacity

For the migration assay, hPSCs in the logarithmic growth phase were collected, and a single-cell suspension was prepared using serum-free medium. The cell density was adjusted to 1×10^5 cells/mL. In the Transwell chamber(3428, Costar, Corning, New York, USA), 800 μL of complete medium was added to the lower chamber, and 200 μL of the cell suspension was added to the upper chamber. The cells were incubated at 37 °C in a 5% CO_2 incubator for 24 hours. After incubation, the Transwell membrane was removed, and the cells on the upper surface of the membrane were gently wiped off with a cotton swab. The membrane was then washed with PBS, fixed in 4% PFA for 30 minutes, and washed again with PBS. The cells were stained with crystal violet for 10 minutes, and the excess stain was washed off. The number of cells that had migrated through the membrane was counted under a microscope in 10 randomly selected high-power fields. The experiment was repeated three times, and the average number of mi-

grated cells was recorded.

For the invasion assay, the steps were similar to the migration assay, except that the upper chamber of the Transwell was pre-coated with a layer of Matrigel matrix. The rest of the procedure followed the same steps as the migration assay. This experiment was also repeated three times, and the average number of invaded cells was recorded.

Conditioned Medium (CM)-Mediated Migration and Invasion Assays of PANC-1 Cells

To evaluate whether treated hPSCs altered their secretory phenotype and consequently affected pancreatic cancer cell progression, CM were collected from the different hPSC groups after the indicated treatments. Briefly, the culture supernatants were collected, centrifuged at 1000 rpm for 5 min to remove cell debris, and used immediately for subsequent assays. PANC-1 cells were suspended in serum-free medium and seeded into the upper chamber of Transwell inserts. A total of 800 μL of the corresponding CM was added to the lower chamber. For the migration assay, uncoated Transwell inserts were used, whereas Matrigel-coated inserts were used for the invasion assay. After incubation for 24 h at 37 °C, cells that migrated or invaded through the membrane were fixed with 4% paraformaldehyde, stained with crystal violet, and counted in 10 randomly selected microscopic fields.

Apoptosis

The apoptosis of hPSCs was detected according to the protocol provided by the Annexin V FITC/PI Apoptosis Detection Kit (G003-1-2, Nanjing Jiancheng Bioengineering Institute, China). Each well of a 6-well culture plate was seeded with 10^5 cells. After 24 hours, the culture medium was discarded, and the wells were washed once with PBS. The respective drugs were then added to each group. After a 24-hour incubation, the cells were harvested by trypsinization and centrifugation, followed by staining with Annexin V and propidium iodide (PI) in the dark for 15 minutes. The apoptosis rate was analyzed using a flow cytometer (CytoFLEX, Beckman Coulter, Brea, California, USA). The gating strategy, compensation settings, and detailed flow cytometry analysis procedures are provided in the **Supplementary Material**. The experiment was repeated three times.

Animals

Forty female BALB/c (nu/nu) mice (6-8 weeks) were purchased from SiPeiFu Biotechnology (Beijing, China). The animal experimental protocol was approved by the Animal Ethics Committee of our Medical University (Approval No. wydw2024-0256), with 12 h of alternating light exposure and free access to water and food. Investigators responsible for outcome measurements were blinded to group allocation whenever feasible.

Fluorescence Imaging

In vivo imaging experiments were conducted to observe the distribution of mPTAs within the body. A subcutaneous injection of a 1:2 mixture of 1.5×10^6 PANC-1 cells and 3×10^6 hPSCs was administered to nude mice. When the tumor volume reached 50 mm^3, five mice were randomly selected for subcutaneous injection of mPTAs, while the remaining five mice were injected with an equal volume of PBS as a control. Fluorescent images were acquired using a PerkinElmer IVIS Spectrum (PerkinElmer, Waltham, Massachusetts, USA) at various time points: before injection, and at 1, 3, 6, 12, and 24 hours post-injection. Anesthesia was induced with 2% isoflurane and maintained at 1–1.5% isoflurane delivered in oxygen throughout the procedure. Following the final imaging time point, mice were euthanized by 5% isoflurane inhalation, followed by cervical dislocation to ensure death. Tumor tissues along with the heart, liver, spleen, lungs, and kidneys were harvested for *ex vivo* fluorescence imaging. The imaging software was used to quantify the fluorescence intensity within selected regions of interest.

Au Biodistribution

To quantitatively evaluate the *in vivo* distribution of mPTAs, ICP-MS (Agilent 8800, Agilent, Santa Clara, California, USA) was performed to determine gold content in tissues. Tumor-bearing mice were subcutaneously injected with mPTAs at the same dose as in the imaging study. At 6, 12, and 24 h post-injection, mice were sacrificed, and tumors and major organs (heart, liver, spleen, lung, and kidney) were harvested and weighed. Tissue samples were digested in aqua regia ($HCl:HNO_3$ = 3:1, 1–2 mL) at 60 °C until complete dissolution. After cooling, samples were diluted to a fixed volume with deionized water. Gold content (^{197}Au) was measured by ICP-MS, and results were expressed as ng Au per gram of tissue (ng/g) based on a standard calibration curve.

Colocalization Analysis of Cy5-siRNA and α-SMA

To further verify the cellular targeting of siRNA within tumors, colocalization analysis of Cy5-labeled siFGF19 with activated PSCs was performed. Tumor tissues were harvested, fixed in 4% PFA, embedded in paraffin, and sectioned (4 μm). After deparaffinization, antigen retrieval was performed, followed by blocking with 5% BSA. Sections were incubated with anti-α-SMA primary antibody (14395-1-AP, Proteintech, China) overnight at 4 °C, followed by incubation with fluorescent secondary antibody. Nuclei were counterstained with DAPI. Fluorescence images were acquired using confocal microscopy.

Safety Assessment

Blood samples were collected at days 0, 5, 10, and 15 via retro-orbital puncture for biochemical analysis to measure the serum levels of alanine aminotransferase (ALT),

aspartate aminotransferase (AST), creatinine (CRE), and blood urea nitrogen (BUN) in mice, thereby evaluating their liver and kidney functions. At the end of the study (day 15), blood collection was performed as the final sampling procedure. Mice were then anesthetized with 5% isoflurane and subsequently euthanized by cervical dislocation following deep anesthesia to ensure humane termination. The harvested heart, liver, spleen, lungs, and kidneys were rinsed with 0.9% saline, fixed in 10% neutral formalin, routinely dehydrated, cleared, embedded in paraffin, and sectioned into thin slices of 4 μm thickness. The sections were deparaffinized with xylene twice and then dehydrated with a graded series of anhydrous ethanol. Hematoxylin staining was performed for 5 minutes, followed by eosin staining for 5 minutes. After mounting with neutral resin and covering with coverslips, the cellular morphology was observed and photographed under a microscope.

Antitumor Experiment

A subcutaneous injection of a 1:2 mixture of 1.5×10^6 PANC-1 cells and 3×10^6 hPSCs was administered to nude mice. The day of injection was designated as day –10. Once the tumor volume reached 50 mm^3, the mice were randomly divided into four groups, with five mice in each group. The groups received subcutaneous injections of siFGF19, mPTAs (equivalent to 4 μg siRNA per mouse), and mPTA (5 mg/kg). Every two days, the body weight and the tumor's longest diameter (a) and shortest diameter (b) of the mice were measured. The tumor volume was calculated using the formula $V = 0.5 \times a \times b^2$. On day 14, all mice were euthanized by 5% isoflurane inhalation followed by cervical dislocation, and the tumors were excised for photography. The tumors were then fixed in 4% paraformaldehyde solution, sectioned, and subjected to hematoxylin and eosin (H&E) staining.

Immunofluorescence Staining of CD8

To evaluate intratumoral immune cell infiltration, immunofluorescence staining for CD8 was performed on tumor tissue sections. Tumor tissues were fixed in 4% PFA, embedded in paraffin, and sectioned (4 μm). After deparaffinization and antigen retrieval, sections were blocked with 5% BSA and incubated overnight at 4 °C with anti-CD8 primary antibody (66868-1-Ig, Proteintech). After washing, samples were incubated with a fluorescent secondary antibody for 1 h at room temperature in the dark. Images were acquired using a fluorescence microscope (ECLIPSE C1, NIKON, Tokyo, Japan).

Statistical Analysis

All data were processed using Excel and analyzed with GraphPad Prism 9 (GraphPad Prism, San Diego, California, USA). software. Quantitative data were expressed as the mean ± standard deviation (SD). Comparisons among multiple groups were performed using one-way analysis of variance followed by Tukey's post hoc test. A value of $p < 0.05$ was considered statistically significant.

Results

Preparation and Characterization of mPTAs

As shown in Fig. 1**A**, mPTAs was successfully synthesized. To verify the encapsulation of siFGF19 within the material, mPTAs was characterized using 1% (w/w) agarose gel electrophoresis. As depicted in the ethidium bromide staining channel of Fig. 1**B**, the band brightness significantly darkened when the ratio of mPTA NPs to siFGF19 was 2:1. With a further increase in the weight ratio, the band disappeared at a 5:1 ratio, indicating successful encapsulation of siFGF19 by mPTA nanoparticles (NPs). Therefore, we selected this ratio of mPTAs for subsequent experiments. TEM results showed that both Au NPs and mPTAs were spherical. The particle size of Au NPs increased significantly after encapsulating siFGF19 and grafting with mPEG-TK (Fig. 1**C**). DLS was used to measure the particle size (Fig. 1**D**) and zeta potential (Fig. 1**E**) of the samples. The results indicated that the particle size and zeta potential of Au NPs were 5.85 ± 0.15 nm and 19.83 ± 0.05 mV, respectively, while the particle size of mPTAs significantly increased and the zeta potential notably decreased to 56.93 ± 0.76 nm and 8.90 ± 1.72 mV, respectively. Additionally, the particle size of mPTAs remained nearly unchanged over seven days (Fig. 1**F**), indicating the high stability of the NPs. As shown in Fig. 1**G**, mPTAs disintegrated into irregular fragments under H_2O_2 stimulation, demonstrating its responsiveness to ROS. Furthermore, the encapsulation of siFGF19 by mPTA NPs protected siFGF19 from degradation by RNase. Upon the addition of H_2O_2, the structure of mPTAs was disrupted, leading to the reappearance of the band (Fig. 1**H**). After incubation of mPTAs with different concentrations of H_2O_2 for 24 h, siFGF19 release was markedly accelerated in the presence of 1 mM H_2O_2, whereas the release was slowest under H_2O_2-free conditions (Fig. 1**I**). TEM images further showed that the well-defined spherical morphology of mPTAs could not be maintained after H_2O_2 treatment (Fig. 1**J**). The successful synthesis of mPEG-TK was confirmed by ^{1}H NMR spectroscopy (Fig. 1**K**), in which the characteristic peak of the mPEG methylene protons (-CH_2-) appeared at 3.5 ppm, and the methyl protons of the TK moiety (-CH_3) were observed near 1.5 ppm. These results indicate that we successfully synthesized a highly stable, ROS-responsive mPTAs that effectively delivers and protects siFGF19.

mPTAs Inhibit H_2O_2-Induced Activation of hPSCs

After co-incubating HUVECs with mPTA NPs at all tested concentrations for 24 hours, cell viability remained above 90% without significant difference between groups, indicating that the mPTA NPs themselves are biocompatible and have no significant cytotoxicity (Fig. 2**A**). Activation of hPSCs is the initiating and key event in the develop-

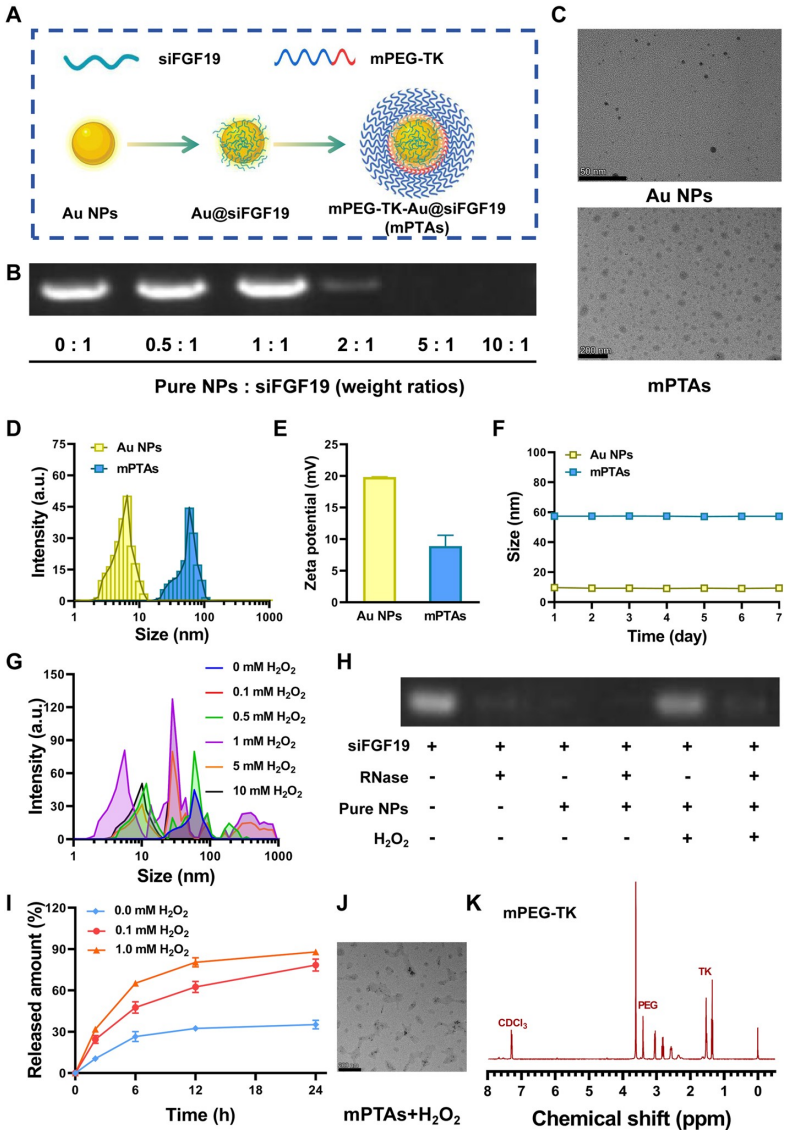

Fig. 1. Preparation and Characterization of mPTAs. (**A**) Schematic diagram of the synthesis process of mPTAs. (**B**) Gel electrophoresis to assess the encapsulation efficiency of siFGF19 at different ratios. (**C**) TEM images of Au NPs and mPTAs (scale bars = 50 nm and 200 nm). (**D**) Particle size of Au NPs and mPTAs. (**E**) Zeta potential of Au NPs and mPTAs. (**F**) Hydrated particle size of mPTAs over seven consecutive days. (**G**) Particle size changes of mPTAs under different concentrations of H_2O_2 (0, 0.1, 0.5, 1, 5, 10 mM). (**H**) Gel electrophoresis verifying the protective and ROS responsiveness of mPTAs against siFGF19. (**I**) Cumulative release profile of siFGF19 from mPTAs in the presence of different concentrations of H_2O_2 over 24 h. (**J**) TEM images showing the morphological changes of mPTAs after 24 h incubation with H_2O_2 (scale bar = 200 nm). (**K**) ^{1}H NMR spectrum of mPEG-TK. Graphs were generated using GraphPad Prism 9, and figure layouts were prepared using Microsoft PowerPoint.

ment of pancreatic fibrosis. Exogenous H_2O_2, a traditional ROS inducer, can promote hPSCs activation and serve as a stimulus for mPTAs responsiveness. However, excessive ROS can damage cells and cause cell death, making it necessary to identify an appropriate activation dose for hPSCs. The results showed that H_2O_2 concentrations ranging from 0 to 100 μM had no significant effect on hPSCs viability, while 200 and 400 μM exhibited noticeable toxicity (Fig. 2**B**, $p < 0.001$). Therefore, 100 μM H_2O_2 was selected for subsequent experiments. Under the stimulation of 100 μM H_2O_2, cell viability decreased in all tested groups, with a clear positive correlation between the extent of decrease and the concentration of mPTAs (Fig. 2**C**). Notably, at only a concentration of 50 µg/mL, mPTAs inhibited hPSCs viability by approximately 50%, further demonstrating the antifibrotic potential of the synthesized mPTAs.

Efficient siRNA-mediated gene silencing requires the successful release of siRNA into the cytoplasm. To facilitate observation, the sense strand of siFGF19 was labeled with Cy5 dye at the 5′ end (Cy5-siFGF19) (excitation/emission wavelengths: 649/670 nm). Compared to free siFGF19, significant red fluorescent signals of Cy5

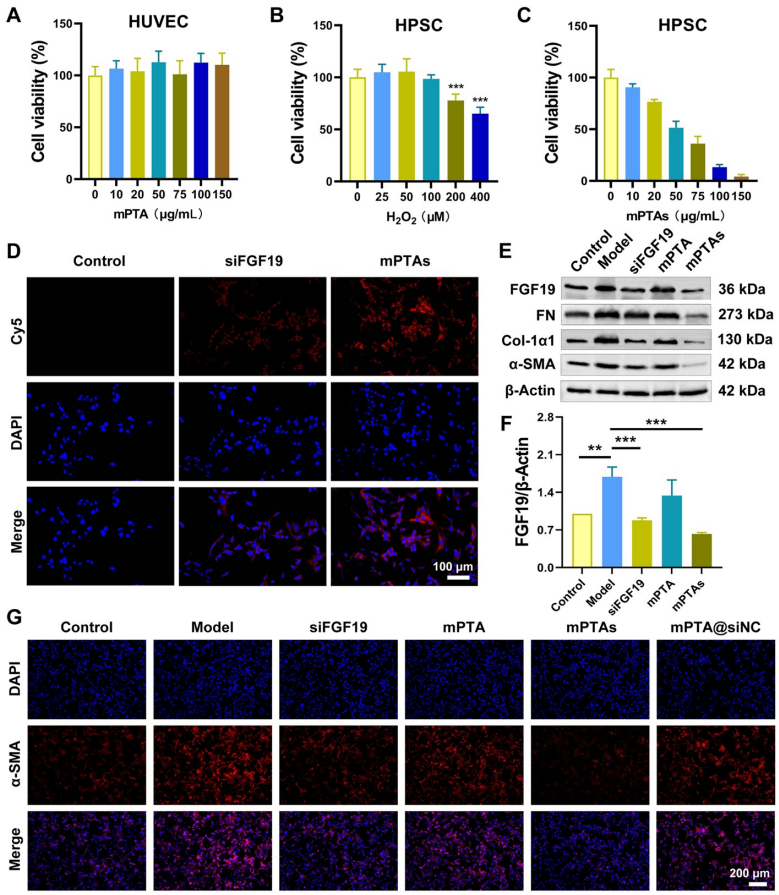

Fig. 2. mPTAs inhibits H_2O_2-induced activation of hPSCs. (**A**) Cytotoxic effects of mPEG-TK-Au (mPTA) (0, 10, 20, 50, 75, 100, and 150 μg/mL) on HUVECs. (**B**) Impact of incubation with different concentrations (0, 25, 50, 100, 200, and 400 μM) of H_2O_2 for 24 hours on the viability of hPSCs. (**C**) Influence of different concentrations (0, 10, 20, 50, 75, 100, and 150 μg/mL) of mPTAs on the viability of hPSCs under stimulation with 100 μM H_2O_2. (**D**) Cellular uptake capability of mPTAs (scale bar = 100 μm). (**E**) and (**F**) Silencing effect of FGF19 as detected by Western blot. (**G**) Immunofluorescence staining of α-SMA (scale bar = 200 μm). Statistical analysis was performed using one-way ANOVA with Tukey's post hoc tests. The data are presented as the means ± SD, n = 3 biological replicates, triplicate technical repeats. *$p < 0.05$, **$p < 0.01$, ***$p < 0.001$. Graphs were generated using GraphPad Prism 9, and figure layouts were prepared using Microsoft PowerPoint.

were observed in the cytoplasm after co-incubation of mPTAs with hPSCs (Fig. 2**D**). This indicates that mPTAs enhances the internalization of siRNA compared to free siRNA. Additionally, the cellular uptake of mPTAs exhibited dose- and time-dependency (Fig. 3**A–D**). Lysosomal co-localization studies showed that mPTAs were internalized by hPSCs after 4 h of incubation, as evidenced by prominent yellow overlapping signals between the red fluorescence of mPTAs and the green fluorescence of LysoTracker. At 8 h, the red fluorescence became more diffusely distributed throughout the cytoplasm, indicating successful endosomal escape and cytosolic release of siFGF19 (Fig. 3**E**). We evaluated the knockdown effect of mPTAs by measuring FGF19 protein and mRNA expression in hPSCs using Western blot and RT-qPCR analyses (Fig. 2**E,F** and **Supplementary Fig. 1A–C**). Compared to the control group, the model group showed a significant increase in FGF19 protein expression ($p = 0.0021$). Both free siFGF19 and mPTAs inhibited FGF19 protein expression compared to the model group ($p < 0.001$), with mPTAs showing a greater inhibitory effect. In contrast, mPTA NPs or mPTA@siNC did not significantly suppress FGF19 expression. Furthermore, we assessed the expression of fibrosis markers in hPSCs by Western blot and RT-qPCR (**Supplementary Fig. 2**). Compared to the control group, the model group showed significantly increased relative expression levels of FN, Col-1α1, and α-SMA mRNA and proteins ($p < 0.05$). Both 50 μg/mL of free siFGF19 and mPTAs significantly reduced the relative expression levels of FN, Col-1α1, and α-SMA mRNA and proteins in the model group ($p < 0.01$). Immunofluorescence staining further confirmed that both free siFGF19 and mPTAs markedly suppressed α-SMA expression in the model group (**Supplementary Fig. 2G**). These data indicate that mPTAs can directly counteract the effects of H_2O_2, thereby inhibiting H_2O_2-induced activation of hPSCs.

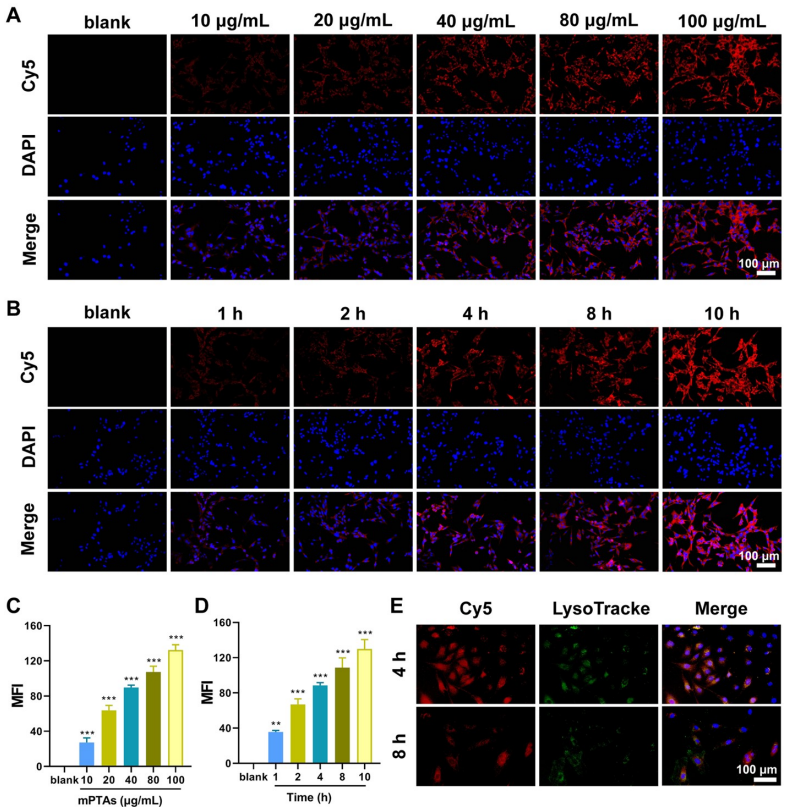

Fig. 3. Cellular uptake, intracellular distribution, and lysosomal escape of mPTAs in hPSCs. Cellular uptake of mPTAs exhibiting dose-dependent (**A**) and time-dependent (**B**) (scale bar = 100 μm). (**C**) Quantitative analysis of fluorescence intensity for dose-dependent uptake. (**D**) Quantitative analysis of fluorescence intensity for time-dependent uptake. (**E**) Lysosomal co-localization of Cy5-labeled mPTAs in hPSCs (scale bar = 100 μm). Statistical analysis was performed using one-way ANOVA with Tukey's post hoc tests. The data are presented as the means ± SD, n = 3 biological replicates, triplicate technical repeats. $^{**}p < 0.01$, $^{***}p < 0.001$, vs. blank group. Graphs were generated using GraphPad Prism 9, and figure layouts were prepared using Microsoft PowerPoint.

mPTAs Inhibits H_2O_2-Induced Proliferation, Migration, and Invasion of Activated hPSCs and Promotes Apoptosis

The proliferation and migration of hPSCs play pivotal roles in the formation of pancreatic fibrosis. Results indicate that H_2O_2 intervention significantly enhances the proliferative capacity of hPSCs, while silencing the FGF19 gene leads to a decrease in their proliferative ability (Fig. 4**A**, $p < 0.001$). The impact of mPTAs on the migration and invasion of hPSCs was assessed using the Transwell assay (Fig. 4**B–D**). We observed that H_2O_2 induces the migration and invasion of hPSCs ($p < 0.001$), while treatment with siFGF19 and mPTAs significantly inhibits cell migration and invasion compared to the model group ($p < 0.001$). Additionally, flow cytometry demonstrated the pro-apoptotic effects of siFGF19 and mPTAs on hPSCs (Fig. 4**E,F** and **Supplementary Fig. 3**). To further assess the influence of inactivated hPSCs on the migratory and invasive behavior of PANC-1 cells, a CM transwell experiment was performed (Fig. 4**G**). Compared with the control group, CM from the mPTAs-treated group significantly suppressed the migration and invasion of PANC-1 cells (Fig. 4**H**). These data suggest that mPTAs inhibit the proliferation, migration, and invasion of H_2O_2-induced activated hPSCs, promote apoptosis, and attenuate the protumorigenic paracrine effects of activated hPSCs on PANC-1 cells, indicating potential stromal-modulating activity.

Antitumor Effects of mPTAs on PANC-1 Subcutaneous Xenograft Tumor

As depicted in Fig. 5**A**, PANC-1 cells and hPSCs were injected into the right flank of Balb/c nude mice to form subcutaneous tumors, and various siRNA formulations (equivalent to 4 μg siRNA per mouse) were administered via subcutaneous injection to evaluate their antitumor effects. Among these formulations, mPTAs exhibited the most significant tumor suppression effect, while the injection of free siRNA showed limited inhibition of tumor growth (Fig. 5**B–D**). During the treatment period, there were no significant differences in body weight among the mice in each group (**Supplementary Fig. 4**), indicating that the drugs did not impose additional burdens on the mice. Furthermore, to further confirm the therapeutic effect, H&E histological analysis was conducted to evaluate the pathological changes in the excised tumors at the end of the treatment. As shown in Fig. 5**E**, compared to the typical morphological features of cancer cells exhibited in

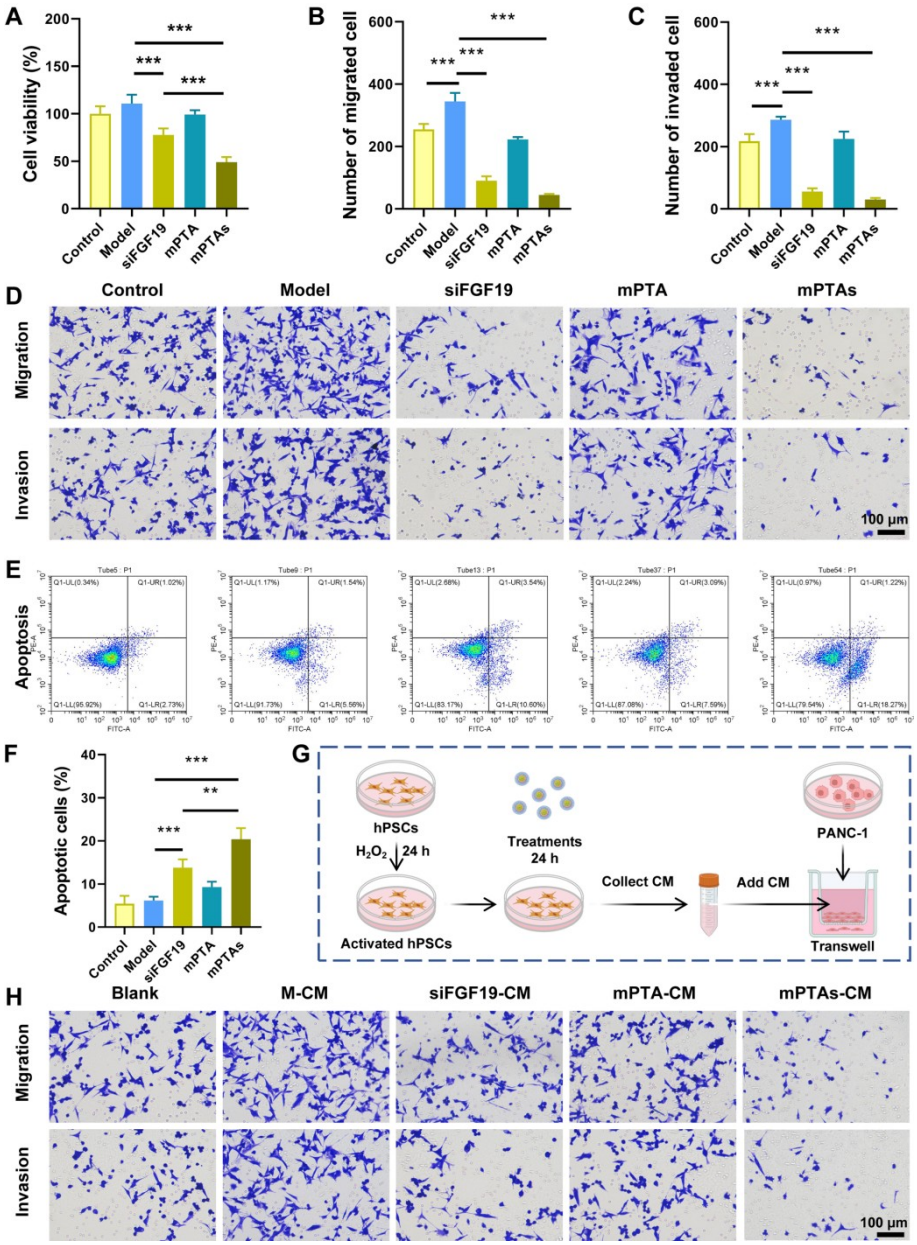

Fig. 4. mPTAs inhibits H_2O_2-induced proliferation, migration, and invasion of activated hPSCs and promotes apoptosis. (**A**) Effect of different materials on the viability of hPSCs. (**B**) Quantification of migrated cells. (**C**) Quantification of invaded cells. (**D**) Representative images of cell migration and invasion (scale bar = 100 μm). (**E**) Representative images of cell apoptosis. (**F**) Quantification of apoptotic cells. (**G**) Schematic illustration of the Transwell co-culture experiment using conditioned medium (CM) from hPSCs with PANC-1 cells. (**H**) Representative images of migration and invasion of PANC-1 cells cultured in conditioned medium (scale bar = 100 μm). Statistical analysis was performed using one-way ANOVA with Tukey's post hoc tests. The data are presented as the means ± SD, n = 3 biological replicates, triplicate technical repeats. $^{**}p < 0.01$, $^{***}p < 0.001$. Graphs were generated using GraphPad Prism 9, and figure layouts were prepared using Microsoft PowerPoint.

other groups (dense arrangement of tumor cells, prominent nucleoli, deep staining, and minimal necrosis), tumors in the mPTAs group showed loose cell arrangement, blurred cell contours, cytoplasmic rupture, and larger areas of tumor cell necrosis, indicating the anti-pancreatic cancer effect of mPTAs. To further elucidate the mechanism by which matrix depletion contributes to tumor inhibition, immunofluorescence staining for CD8 was performed to assess immune cell infiltration. The results revealed significantly enhanced $CD8^+$ T cell infiltration in the mPTAs group, while no notable changes were observed in the free siFGF19 or blank mPTA groups (Fig. 5**F**). Additionally, to confirm hPSC inactivation and stromal remodeling, the expression levels of FGF19, α-SMA, Collagen I, and FN in tumor tissues were examined by immunofluorescence (Fig. 5**G** and **Supplementary Fig. 5**). Compared with the control group,

mPTAs treatment significantly reduced the expression of FGF19, α-SMA, Collagen I, and FN. These findings indicate that mPTAs successfully silenced FGF19 expression *in vivo*, leading to hPSC inactivation and subsequent stromal remodeling.

Biodistribution and Safety Evaluation of mPTAs in vivo

To further confirm the feasibility of *in vivo* application of mPTAs, its targeting and safety need to be validated. *In vivo* imaging results in mice demonstrate that after subcutaneous injection of Cy5-labeled mPTAs (equivalent to 4 μg siRNA per mouse), abundant fluorescence is detected in the tumor, peaking at 12 hours and gradually diminishing thereafter (Fig. 6**A,B**). Subsequently, *ex vivo* imaging of the mouse heart, liver, spleen, lung, kidney, and tumor tissues was conducted. The results reveal that the fluorescence intensity is highest in the tumor, with the highest accumulation of mPTAs, followed by accumulation in the liver and kidney, indicating its certain controlled release capability (Fig. 6**C,D**). To quantitatively analyze the biodistribution, the Au content in tumor tissues and major organs was measured at 6, 12, and 24 h after injection. The Au content in tumors reached its peak at 12 h, consistent with the Cy5 fluorescence imaging results. Moderate Au accumulation was also observed in the liver, kidney, and spleen (Fig. 6**E**). To verify whether mPTAs could deliver siFGF19 to PSCs *in vivo*, immunofluorescence co-localization analysis of Cy5-labeled siRNA and α-SMA was performed. As shown in Fig. 6**F**, free siRNA exhibited weak, scattered, and diffuse red fluorescence signals. In contrast, mPTAs-treated tumors displayed bright, punctate red fluorescence signals that were predominantly localized within α-SMA-positive regions, indicating successful delivery of siFGF19 into target PSCs.

Blood biochemical analysis targeting liver and kidney function shows no significant changes in ALT, AST, CRE, and BUN levels in mice injected with mPTAs on days 5, 10, and 15 (Fig. 6**G**). Importantly, compared to the PBS (negative control) group, no significant pathological changes are observed in the heart, liver, spleen, lung, or kidney of mice 15 days after injection of mPTAs (Fig. 6**H**). This indicates the excellent *in vivo* biosafety of mPTAs and its potential for *in vivo* applications.

Discussion

In the present study, we developed a ROS-responsive gold nanoparticle-based siRNA delivery system and demonstrated its ability to effectively reprogram PSCs and suppress tumor progression in PDAC. Rather than focusing solely on tumor cell cytotoxicity, our strategy specifically targets the stromal compartment, addressing one of the key barriers to effective PDAC therapy-desmoplastic fibrosis.

A central finding of this work is that silencing FGF19 significantly attenuates PSC activation and reduces the expression of key fibrotic markers, including α-SMA, collagen I, and FN. These results suggest that FGF19 appears to be associated with stromal activation in PSCs and may participate in the regulation of stromal activation. By targeting FGF19, our system effectively reprograms PSCs from an activated, pro-fibrotic state toward a less active phenotype, thereby disrupting the pathological tumor-stroma interaction.

Efficient intracellular delivery remains a major challenge for RNAi therapeutics. In this study, the incorporation of Au NPs enabled stable loading and protection of siFGF19, while surface modification with mPEG-TK provided ROS-responsive release capability. Under oxidative conditions mimicking the tumor microenvironment, the cleavage of TK linkages facilitated the controlled release of siRNA, leading to enhanced gene silencing efficiency. Compared with free siRNA, the nanoplatform significantly improved cellular uptake and intracellular availability, highlighting the importance of stimuli-responsive delivery systems in overcoming biological barriers.

Importantly, the biological effects observed in PSCs extend beyond gene silencing and include changes in cellular behavior. FGF19 knockdown significantly suppressed PSC proliferation, migration, and invasive capacity, while promoting apoptotic signaling under oxidative stress conditions. These coordinated effects suggest that targeting FGF19 not only interrupts a single signaling pathway but also induces a broader phenotypic shift in PSC biology. Such stromal reprogramming is increasingly recognized as a more effective therapeutic strategy than complete stromal ablation, which may paradoxically accelerate tumor progression in certain contexts.

PSCs are located in the interlobular spaces and around the acini of the pancreas, surrounding neighboring acinar cell bases. They are resident cells in the pancreas and exist mainly in a quiescent state in healthy individuals [24,25]. When the pancreas is subjected to stimuli such as alcohol or ROS, damage, inflammation, or carcinogenesis may occur. Injured acinar cells, inflammatory cells, pancreatic cancer cells, and others can release large amounts of inflammatory factors, growth factors, sonic hedgehog, and other substances, causing PSCs to transition from a quiescent state to an activated state resembling myofibroblasts [26]. Activated PSCs express α-SMA, proliferate rapidly, migrate, synthesize, and secrete large amounts of extracellular matrix components such as type I collagen, type III collagen, FN, etc., which play important roles in the growth and invasion of pancreatic cancer cells [27,28]. Yan *et al*. [29] confirmed that H_2O_2-induced ROS promotes the expression of α-SMA in PSCs, consistent with our results. Our data also showed that both siFGF19 and mPTAs significantly reduced the activation level of hPSCs in the presence of H_2O_2, but mPTAs was more effective than free siFGF19. This may be attributed to the effective protection and delivery of siFGF19 by mPTA NPs, enabling it to stably exist within cells and exert gene silencing effects. Furthermore,

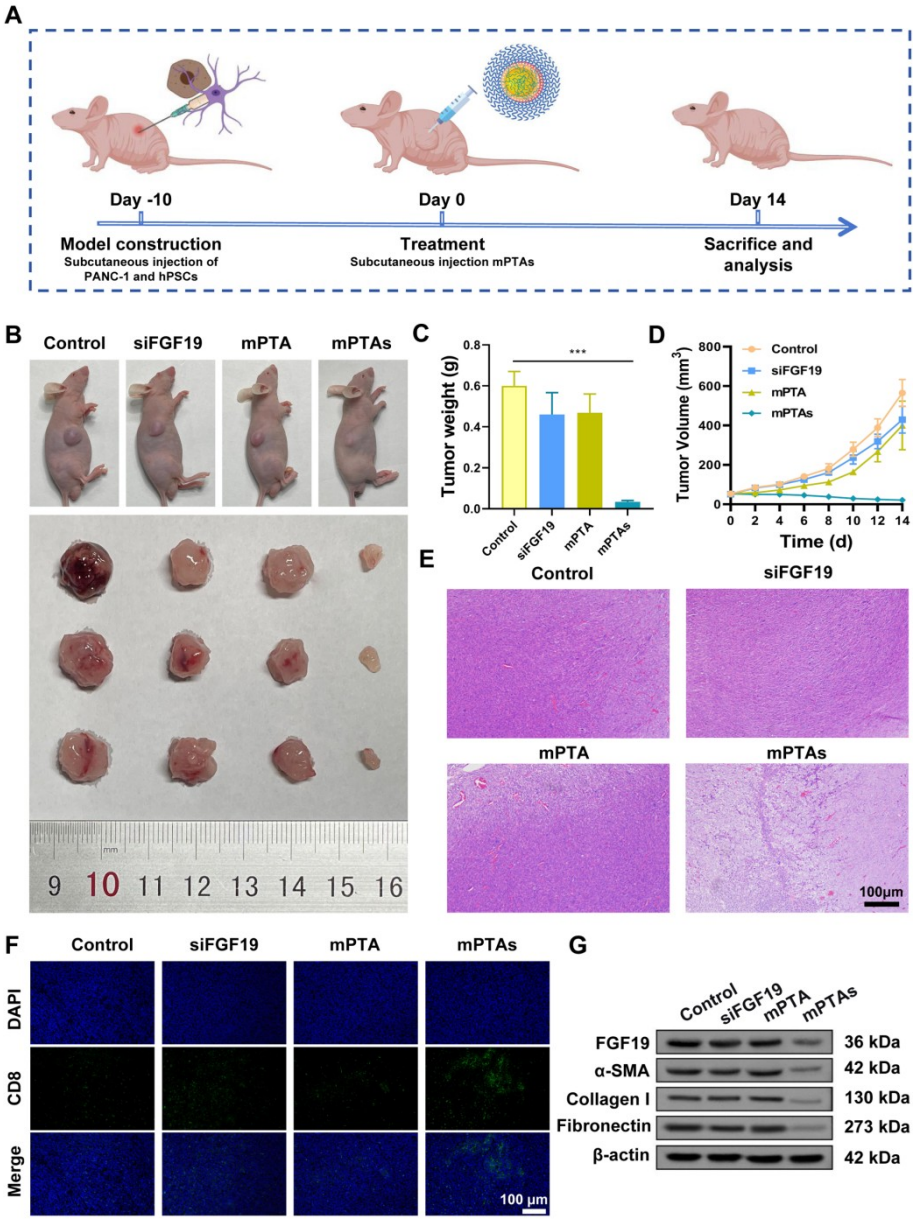

Fig. 5. Antitumor effects of mPTAs on PANC-1 subcutaneous graft tumor. (**A**) Schematic diagram of subcutaneous xenograft tumor model experiments. (**B**) Representative images of tumor-bearing mice and isolated tumors. (**C**) Tumor weight of mice at the time of sacrifice. (**D**) Mouse tumor volume curve. (**E**) Hematoxylin and eosin staining analysis of tumor tissues. (**F**) Immunofluorescence analysis of CD8 expression in tumor tissues (scale bar = 100 μm). (**G**) Expression levels of FGF19, α-SMA, Collagen I, and Fibronectin in tumor tissues. Statistical analysis was performed using one-way ANOVA with Tukey's post hoc tests. The data are presented as the means ± SD, n = 5. ***$p < 0.001$. Graphs were generated using GraphPad Prism 9, and figure layouts were prepared using Microsoft PowerPoint.

Western blot and qPCR results consistently show that mPTAs significantly downregulates the expression of fibrotic markers (FN, Col-1α1, and α-SMA), further confirming its anti-fibrotic potential. Additionally, we observed that siFGF19 and mPTAs have significant inhibitory effects on H_2O_2-induced proliferation, migration, and invasion of hPSCs, and can promote hPSCs apoptosis.

The targeting effect of nanocarriers is crucial for improving therapeutic efficacy, reducing dosage, and minimizing toxicity [30]. The *in vivo* results further demonstrated that mPTAs preferentially accumulated in tumor tissues and exhibited a favorable safety profile. The observed tumor inhibition is likely attributable not only to direct gene silencing effects but also to alterations in the fibrotic stromal compartment, suggesting partial remodeling of the tumor stroma. Notably, while the enhanced permeability and retention effect may contribute to nanoparticle accumulation, its heterogeneity and limited clinical predictabil-

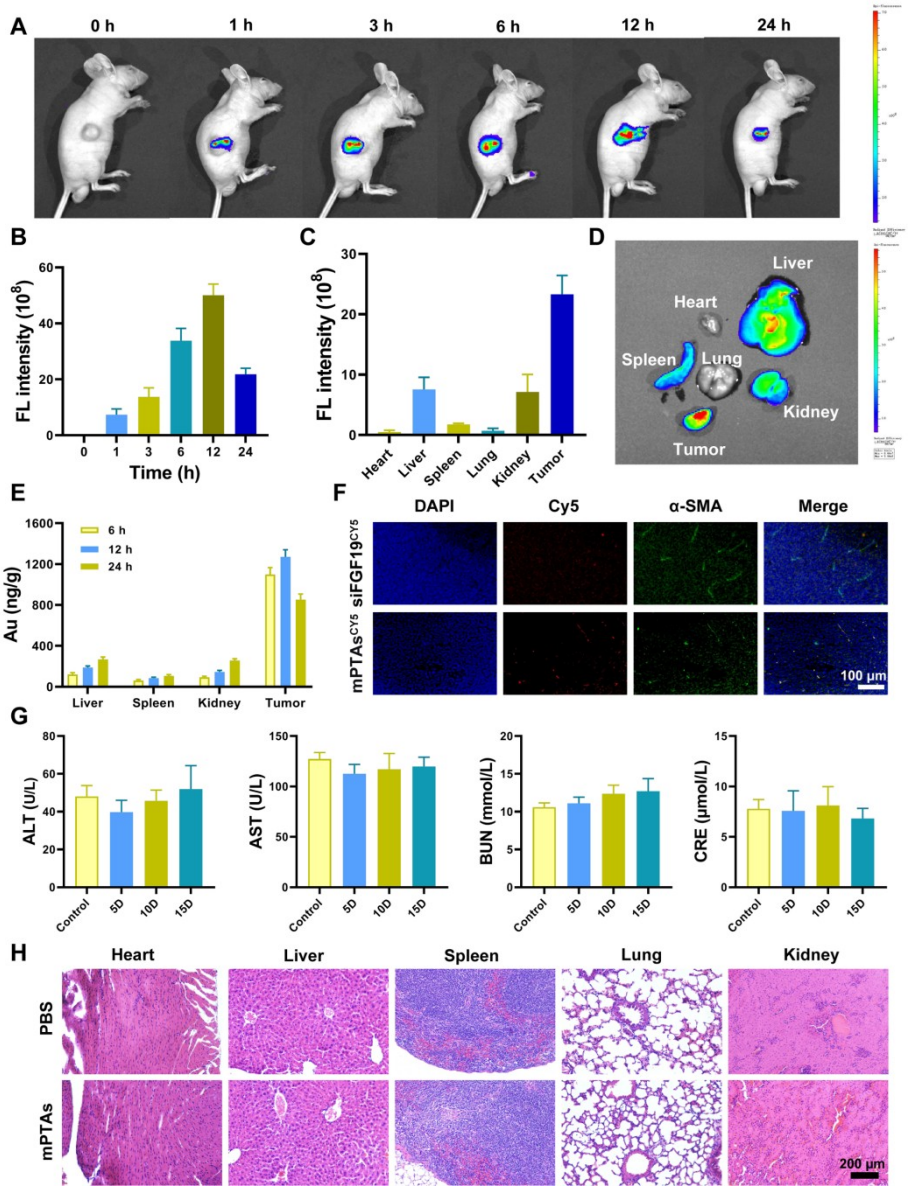

Fig. 6. Biodistribution and safety evaluation of mPTAs *in vivo*. (**A**) and (**B**) Accumulation of mPTAs in tumor-bearing mice over 24 hours. (**C**) and (**D**) Distribution of mPTAs in heart, liver, spleen, lung, kidney, and tumor tissues 24 hours after subcutaneous injection. (**E**) Quantitative analysis of Au content in major organs and tumors at different time points. (**F**) Immunofluorescence co-localization of Cy5-labeled siFGF19 with α-SMA-positive activated PSCs in tumor tissues (scale bar = 100 μm). (**G**) Assessment of liver and kidney indicators. (**H**) Hematoxylin and eosin staining of heart, liver, spleen, lung, and kidney tissues (scale bar = 200 μm). The data are presented as the means ± SD, n = 5. Graphs were generated using GraphPad Prism 9, and figure layouts were prepared using Microsoft PowerPoint.

ity have been increasingly recognized [31,32]. Therefore, the ROS-responsive release mechanism employed in this study provides an additional layer of targeting specificity beyond passive accumulation. Recent advances in nanomedicine have highlighted the importance of integrating microenvironment-responsive features with molecular targeting strategies. Compared with conventional nanocarriers, our system combines ROS-triggered release with gene-specific silencing, offering a dual-functional approach to modulate both cellular behavior and extracellular matrix dynamics. This approach is particularly relevant for PDAC, where dense stroma plays a dominant role in therapeutic resistance.

Despite achieving significant experimental results, this study also has some limitations and areas that need further optimization. First, the long-term stability of nanoparticles and their *in vivo* metabolic pathways require further investigation. Long-term *in vivo* safety and pharmacokinetic studies are necessary to evaluate the potential and safety of this therapeutic strategy in clinical applications.

Second, although our study demonstrates effective stromal modulation, the impact of this strategy on immune components within the tumor microenvironment remains unclear and warrants further exploration. Given the emerging interplay between stromal remodeling and antitumor immunity, future studies integrating this nanoplatform with immunotherapeutic approaches may yield synergistic benefits.

Conclusions

In conclusion, this study presents a ROS-responsive siRNA nanoplatform that effectively targets the FGF19-driven stromal axis and reprograms PSC activation in PDAC. By simultaneously addressing gene dysregulation and microenvironmental barriers, this strategy provides a promising framework for the development of next-generation nanomedicines aimed at overcoming stromal resistance in solid tumors.

List of Abbreviation

PDAC, pancreatic ductal adenocarcinoma; PSCs, pancreatic stellate cells; FGF19, fibroblast growth factor 19; siRNA, small interfering RNA; hPSCs, human pancreatic stellate cells; FN, fibronectin; RNAi, RNA interference; Au NPs, gold nanoparticles; TK, thioketal; mPEG, methoxy polyethylene glycol; NHS, N-hydroxy succinimide; EDC·HCl, N-(3-Dimethylaminopropyl)-N′-ethylcarbodiimide hydrochloride; TEM, transmission electron microscopy; mPTA, mPEG-TK-Au; mPTAs, mPEG-TK-Au@siFGF19; FBS, fetal bovine serum; HUVECs, human umbilical vein endothelial cells; CCK-8, Cell Counting Kit-8; PFA, paraformaldehyde; Col-1α1, collagen type I alpha 1; RIPA, radioimmunoprecipitation assay; ECL, enhanced chemiluminescence; α-SMA, α-smooth muscle actin; RT-qPCR, reverse transcription quantitative polymerase chain reaction; CM, conditioned medium; PI, propidium iodide; ALT, alanine aminotransferase; AST, aspartate aminotransferase; CRE, creatinine; BUN, blood urea nitrogen; H&E, hematoxylin and eosin; SD, standard deviation; ANOVA, analysis of variance; ROS, reactive oxygen species; Cy5, Cyanine 5.

Availability of Data and Materials

The data that support the findings of this study are available from the corresponding authors upon reasonable request.

Author Contributions

ZHW and SHZ contributed to the conceptualization, design and implementation of the research and wrote the manuscript. SZL contributed to the conceptualization and funding acquisition, and reviewed the manuscript. ZHW, SHZ, ZRT, XHZ, XCZ, SDL, BEW, and YLX contributed to the interpretation of data. ZRT, XHZ, and XCZ contributed to the data analysis. HFT, QYZ, and ZLN reviewed the manuscript and supervised the project. All authors read and approved the final manuscript.

Ethics Approval and Consent to Participate

The animal experiments were approved by the Experimental Animal Ethics Committee of Wenzhou Medical University (wydw2024-0256).

Acknowledgments

None.

Funding

This work was supported by the Joint TCM Science & Technology Projects of National Demonstration Zones for Comprehensive TCM Reform (Zhengjiang Province) (No:GZY-KJS-ZJ-2026-082), Key Program of Natural Science Foundation of Zhejiang Province (No:LZ24H280004), Leading Geese Plan of Zhejiang Province (No:2026C02A1086), Hainan Province Science and Technology Special Fund (No:ZDYF2026LCLH010), and the Zhejiang Provincial Health and Wellness Industry Science and Technology Project (No:2026767977).

Conflict of Interest

The authors declare no conflict of interest.

Supplementary Material

Supplementary material associated with this article can be found, in the online version, at https://doi.org/10.22203/eCM.v058a14.

References

[1] Backx E, Coolens K, Van den Bossche JL, Houbracken I, Espinet E, Rooman I. On the Origin of Pancreatic Cancer: Molecular Tumor Subtypes in Perspective of Exocrine Cell Plasticity. Cellular and Molecular Gastroenterology and Hepatology. 2022; 13: 1243–1253. https://doi.org/10.1016/j.jcmgh.2021.11.010.

[2] Halbrook CJ, Lyssiotis CA, Pasca di Magliano M, Maitra A. Pancreatic cancer: Advances and challenges. Cell. 2023; 186: 1729–1754. https://doi.org/10.1016/j.cell.2023.02.014.

[3] Sherman MH, Beatty GL. Tumor Microenvironment in Pancreatic Cancer Pathogenesis and Therapeutic Resistance. Annual Review of Phytopathology. 2023; 18: 123–148. https://doi.org/10.1146/annurev-pathmechdis-031621-024600.

[4] Murray ER, Menezes S, Henry JC, Williams JL, Alba-Castellón L, Baskaran P, *et al*. Disruption of pancreatic stellate cell myofibroblast phenotype promotes pancreatic tumor invasion. Cell Reports. 2022; 38: 110227. https://doi.org/10.1016/j.celrep.2021.110227.

[5] Hessmann E, Buchholz SM, Demir IE, Singh SK, Gress TM, Ellenrieder V, *et al*. Microenvironmental Determinants of Pancreatic Cancer. Physiological Reviews. 2020; 100: 1707–1751. https://doi.org/10.1152/physrev.00042.2019.

[6] Ramakrishnan P, Loh WM, Gopinath SCB, Bonam SR, Fareez IM, Mac Guad R, *et al*. Selective phytochemicals targeting pancreatic stellate cells as new anti-fibrotic agents for chronic pancreatitis and pancreatic cancer. Acta Pharmaceutica Sinica B. 2020; 10: 399–413. https://doi.org/10.1016/j.apsb.2019.11.008.

[7] Hosein AN, Brekken RA, Maitra A. Pancreatic cancer stroma: an update on therapeutic targeting strategies. Nature Reviews Gastroenterology & Hepatology. 2020; 17: 487–505. https://doi.org/10.1038/s41575-020-0300-1.

[8] Qi L, Duan BW, Wang H, Liu YJ, Han H, Han MM, *et al*. Reactive Oxygen Species-Responsive Nanoparticles Toward Extracellular Matrix Normalization for Pancreatic Fibrosis Regression. Advanced Science. 2024; 11: e2401254. https://doi.org/10.1002/advs.202401254.

[9] Phan P, Saikia BB, Sonnaila S, Agrawal S, Alraawi Z, Kumar TKS, *et al*. The Saga of Endocrine FGFs. Cells. 2021; 10: 2418. https://doi.org/10.3390/cells10092418.

[10] Schumacher JD, Kong B, Wu J, Rizzolo D, Armstrong LE, Chow MD, *et al*. Direct and Indirect Effects of Fibroblast Growth Factor (FGF) 15 and FGF19 on Liver Fibrosis Development. Hepatology. 2020; 71: 670–685. https://doi.org/10.1002/hep.30810.

[11] Chia L, Wang B, Kim JH, Luo LZ, Shuai S, Herrera I, *et al*. HMGA1 induces FGF19 to drive pancreatic carcinogenesis and stroma formation. The Journal of Clinical Investigation. 2023; 133: e151601. https://doi.org/10.1172/JCI151601.

[12] Kara G, Calin GA, Ozpolat B. RNAi-based therapeutics and tumor targeted delivery in cancer. Advanced Drug Delivery Reviews. 2022; 182: 114113. https://doi.org/10.1016/j.addr.2022.114113.

[13] Hu B, Zhong L, Weng Y, Peng L, Huang Y, Zhao Y, *et al*. Therapeutic siRNA: state of the art. Signal Transduction and Targeted Therapy. 2020; 5: 101. https://doi.org/10.1038/s41392-020-0207-x.

[14] Khan S, Rehman U, Parveen N, Kumar S, Baboota S, Ali J. siRNA therapeutics: insights, challenges, remedies and future prospects. Expert Opinion on Drug Delivery. 2023; 20: 1167–1187. https://doi.org/10.1080/17425247.2023.2251890.

[15] Zhang J, Mou L, Jiang X. Jiang. Surface chemistry of gold nanoparticles for health-related applications. Chemical Science. 2020; 11: 923–936. https://doi.org/10.1039/c9sc06497d.

[16] Hosseini SA, Kardani A, Yaghoobi H. Yaghoobi. A comprehensive review of cancer therapies mediated by conjugated gold nanoparticles with nucleic acid. International Journal of Biological Macromolecules. 2023; 253: 127184. https://doi.org/10.1016/j.ijbiomac.2023.127184.

[17] Xue C, Hu S, Gao ZH, Wang L, Luo MX, Yu X, *et al*. Programmably tiling rigidified DNA brick on gold nanoparticle as multi-functional shell for cancer-targeted delivery of siRNAs. Nature Communications. 2021; 12: 2928. https://doi.org/10.1038/s41467-021-23250-5.

[18] Yang Y, Han Y, Sun Q, Cheng J, Yue C, Liu Y, *et al*. Au-siRNA@ aptamer nanocages as a high-efficiency drug and gene delivery system for targeted lung cancer therapy. Journal of nanobiotechnology. 2021; 19: 54. https://doi.org/10.1186/s12951-020-00759-3.

[19] Hao Y, Chen Y, He X, Yu Y, Han R, Li Y, *et al*. Polymeric Nanoparticles with ROS-Responsive Prodrug and Platinum Nanozyme for Enhanced Chemophotodynamic Therapy of Colon Cancer. Advanced Science. 2020; 7: 2001853. https://doi.org/10.1002/advs.202001853.

[20] Yu H, Jin F, Liu D, Shu G, Wang X, Qi J, *et al*. ROS-responsive nano-drug delivery system combining mitochondria-targeting ceria nanoparticles with atorvastatin for acute kidney injury. Theranostics. 2020; 10: 2342–2357. https://doi.org/10.7150/thno.40395.

[21] Li X, Li Y, Yu C, Bao H, Cheng S, Huang J, *et al*. ROS-Responsive Janus Au/Mesoporous Silica Core/Shell Nanoparticles for Drug Delivery and Long-Term CT Imaging Tracking of MSCs in Pulmonary Fibrosis Treatment. ACS Nano. 2023; 17: 6387–6399. https://doi.org/10.1021/acsnano.2c11112.

[22] Li R, Xie H, Zhang C, Sun Y, Yin H. ROS-Responsive Polymeric Micelle for Improving Pesticides Efficiency and Intelligent Release. Journal of Agricultural and Food Chemistry. 2020; 68: 9052–9060. https://doi.org/10.1021/acs.jafc.0c03856.

[23] Jiang Z, Wang H, Zhang Z, Pan J, Yuan H. Cartilage targeting therapy with reactive oxygen species-responsive nanocarrier for osteoarthritis. Journal of nanobiotechnology. 2022; 20: 419. https://doi.org/10.1186/s12951-022-01629-w.

[24] Pothula SP, Pirola RC, Wilson JS, Apte MV. Pancreatic stellate cells: Aiding and abetting pancreatic cancer progression. Pancreatology. 2020; 20: 409–418. https://doi.org/10.1016/j.pan.2020.01.003.

[25] Feng H, Moriyama T, Ohuchida K, Sheng N, Iwamoto C, Shindo K, *et al*. N-acetyl cysteine induces quiescent-like pancreatic stellate cells from an active state and attenuates cancer-stroma interactions. Journal of Experimental and Clinical Cancer Research. 2021; 40: 133. https://doi.org/10.1186/s13046-021-01939-1.

[26] Jin G, Hong W, Guo Y, Bai Y, Chen B. Molecular Mechanism of Pancreatic Stellate Cells Activation in Chronic Pancreatitis and Pancreatic Cancer. Journal of Cancer. 2020; 11: 1505–1515. https://doi.org/10.7150/jca.38616.

[27] Mercanti L, Sindaco M, Mazzone M, Di Marcantonio MC, Piscione M, Muraro R, *et al*. PDAC, the Influencer Cancer: Cross-Talk with Tumor Microenvironment and Connected Potential Therapy Strategies. Cancers. 2023; 15: 2923. https://doi.org/10.3390/cancers15112923.

[28] Belhabib I, Zaghdoudi S, Lac C, Bousquet C, Jean C. Extracellular Matrices and Cancer-Associated Fibroblasts: Targets for Cancer Diagnosis and Therapy? Cancers. 2021; 13: 3466. https://doi.org/10.3390/cancers13143466.

[29] Yan B, Cheng L, Jiang Z, Chen K, Zhou C, Sun L, *et al*. Resveratrol Inhibits ROS-Promoted Activation and Glycolysis of Pancreatic Stellate Cells via Suppression of miR-21. Oxidative Medicine and Cellular Longevity. 2018; 2018: 1346958. https://doi.org/10.1155/2018/1346958.

[30] Tian H, Zhang T, Qin S, Huang Z, Zhou L, Shi J, *et al*. Enhancing the therapeutic efficacy of nanoparticles for cancer treatment using versatile targeted strategies. Journal of Hematology & Oncology. 2022; 15: 132. https://doi.org/10.1186/s13045-022-01320-5.

[31] Fang J, Islam W, Maeda H. Exploiting the dynamics of the EPR effect and strategies to improve the therapeutic effects of nanomedicines by using EPR effect enhancers. Advanced Drug Delivery Reviews. 2020; 157: 142–160. https://doi.org/10.1016/j.addr.2020.06.005.

[32] Zi Y, Yang K, He J, Wu Z, Liu J, Zhang W. Strategies to enhance drug delivery to solid tumors by harnessing the EPR effects and alternative targeting mechanisms. Advanced Drug Delivery Reviews. 2022; 188: 114449. https://doi.org/10.1016/j.addr.2022.114449.

Editor's note: The Scientific Editors responsible for this paper were Xiaoyuan Ji and Kelong Fan.

Received: 30th April 2026; **Accepted**: 23rd July 2026; **Published**: 31st August 2026